

ARTICLE OPEN



Boosting effect of strong western pole of the Indian Ocean Dipole on the decay of El Niño events

Jia Wu^{1,2}, Hanjie Fan¹, Shuheng Lin^{1,2}, Wenxiu Zhong^{1,2}, Shan He³, Noel Keenlyside^{4,5,6} and Song Yang^{1,2}✉

The Indian Ocean Basin (IOB) mode is believed to favor the decay of El Niño via modulating the zonal wind anomalies in the western equatorial Pacific, while the contribution of the Indian Ocean Dipole (IOD) mode to the following year's El Niño remains highly controversial. In this study, we use the evolution of fast and slow decaying El Niño events during 1950–2020 to demonstrate that the positive IOD with a strong western pole prompts the termination of El Niño, whereas a weak western pole has no significant effect. The strong western pole of a positive IOD leads to a strong IOB pattern peaking in the late winter (earlier than normal), enhancing local convection and causing anomalous rising motions over the tropical Indian Ocean and sinking motions over the western tropical Pacific. The surface equatorial easterly wind anomalies on the western flank of the sinking motions stimulate oceanic equatorial upwelling Kelvin waves, which shoal the thermocline in the eastern equatorial Pacific and rapidly terminate the equatorial warming during El Niño. However, a weak western pole of the IOD induces a weak IOB mode that peaks in the late spring, and the above-mentioned cross-basin physical processes do not occur.

npj Climate and Atmospheric Science (2024)7:6; <https://doi.org/10.1038/s41612-023-00554-5>

INTRODUCTION

Understanding the characteristics and causes of ENSO decay has received tremendous attentions in the climate research community^{1–3} because the duration of El Niño–Southern Oscillation (ENSO) events varies substantially. This variation controls the persistence of ENSO-associated teleconnections, which strongly modulates global climate anomalies^{4–6}. One of the most well-known characteristics reported by previous studies is the asymmetric decay of El Niño and La Niña, namely, the rapid (slow) decay of El Niño (La Niña)^{7–9}. Chen et al.¹⁰, however, classified about 40% of the El Niño events during 1950–2020 as slow decaying events, which deviated from the common knowledge that El Niño usually terminates fast in the boreal summer after peaking in winter. Thus, examining of the fast and slow decaying El Niño events separately is essential to obtain a more comprehensive understanding of the factors that contribute to the termination of El Niño.

In recent years, the inter-basin interactions between various oceans have been emphasized in elucidating the mechanisms for El Niño decay^{11,12}, especially the role of the Indian Ocean^{13–15}. Based on composite analyses of all El Niño events, previous studies have revealed the importance of surface zonal wind anomalies over the western equatorial Pacific in modulating El Niño decaying processes^{16,17}. Further investigations have indicated that the Indian Ocean Basin (IOB) warming can induce surface easterly wind anomalies over the western equatorial Pacific¹⁸, which act to terminate El Niño via adjusting oceanic dynamic processes^{19,20}.

Researchers have also attempted to explore whether the Indian Ocean Dipole (IOD) mode can affect the following year's El Niño by using observations and numerical model experiments^{21–23}. A positive IOD in autumn can perturb the Indo-Pacific Walker circulation to generate surface westerly wind anomalies over the

western-central equatorial Pacific; and through the Bjerknes feedback these lead to negative sea surface temperature (SST) anomalies^{23,24}. Although these surface westerly wind anomalies relax when the IOD disappears, the negative SST anomalies can be amplified persistently, thereby conducive to the development of La Niña in the following year. However, Atmospheric General Circulation Model (AGCM) experiments showed that no significant wind anomalies occur in the western equatorial Pacific during the IOD period²⁵. This is presumably because the impacts from the eastern and western poles of the IOD cancel^{26,27}. To reconcile the above-mentioned contradictory viewpoints, researchers compared the IOD–IOB combined forcing experiments and pure IOB forcing experiments; they revealed that the abrupt collapse of the IOD eastern pole could facilitate the fast growth of IOB-caused westerly wind anomalies in the western equatorial Pacific, leading to a faster termination of El Niño²⁸. While these interactions can explain the negative correlation between boreal-autumn IOD and ENSO in the following year, other researchers have suggested the relationship is a statistical artifact of the ENSO cycle, which does not provide additional predictability for the ENSO in the following year²².

Despite many progresses, the impact of the IOD on El Niño decay is not fully understood. First, it is still debatable whether the IOD–ENSO relationship signifies a physical impact of the IOD on the subsequent ENSO^{23,28}, or if it is simply a mathematical connection arising from the autocorrelation of ENSO²². Second, Izumo et al.^{23,28} placed a greater emphasis on the role of the IOD eastern pole, but paid less attention to the western pole, which was suggested to counteract the impact of the eastern pole²⁵. In addition, the intensity and coverage area of the both poles are not always similar to each other^{29–32}. Yet, few analyses have been conducted to identify the possible effect of the western pole. Third, earlier studies primarily relied on composite analyses of all

¹School of Atmospheric Sciences, Sun Yat-sen University; Southern Marine Science and Engineering Guangdong Laboratory (Zhuhai), Zhuhai, China. ²Guangdong Province Key Laboratory for Climate Change and Natural Disaster Studies, Sun Yat-sen University, Zhuhai, China. ³School of Marine Sciences, Sun Yat-sen University, Zhuhai, China. ⁴Geophysical Institute, University of Bergen, Bergen, Norway. ⁵Bjerknes Centre for Climate Research, University of Bergen, Bergen, Norway. ⁶Nansen Environmental and Remote Sensing Centre, Bergen, Norway. ✉email: yangsong3@mail.sysu.edu.cn

El Niño events to examine the associated physical processes for how an IOD induces zonal wind anomalies in the western equatorial Pacific^{33,34}. However, this approach may blur valuable clues due to the inclusion of both fast and slow decaying El Niño events.

In this study, we revisit the impact of the IOD on El Niño decay, by focusing on diverse states of the western and eastern poles of the IOD during fast and slow decaying El Niño events. Most of the published studies discussed the impacts of the IOD or the IOB on El Niño decay separately; we seek to provide a more comprehensive understanding of the combined impact of these two Indian Ocean modes on El Niño decay. Specifically, building on the consensus of the predominant fuel effect of the ENSO on the development of the IOB^{35–37}, we propose a modulation effect of the IOD, especially the western pole as the precursor background of the IOB, on the strength and peaking phase of the IOB and the subsequent El Niño decay.

RESULTS

Discrepancies between fast and slow decaying El Niño events

As previously documented³⁸, El Niño usually reaches its peak in the boreal winter and turns into La Niña in the following summer (Fig. 1a, purple curve). We identify fast decaying (FD) and slow decaying (SD) El Niño events based on the temporal evolution of Niño-3.4 SST anomalies during 1950–2020 (Fig. 1), through comparing the difference in Niño-3.4 index between the peaking winter and the decaying summer (June–July–August (JJA)) and checking if the JJA Niño-3.4 SST anomalies in the decaying year decline to non-ENSO state. Fifteen FD cases and ten SD cases are clearly distinguished by the classification criteria (Fig. 1b; detailed criteria in the “Methods” section). Compared to the composite evolution for all El Niño events, the composite time series of FD and SD El Niño events evolve almost synchronously during the developing phase. However, during the decaying phase the FD events experience a phase transition before May, whereas the composite Niño-3.4 index for SD events remains positive in the year following its peak phase (Fig. 1a, orange and blue curves).

The spatial distribution of composite SST anomalies provides a clearer picture of the evolution of FD and SD El Niño events (Fig. 2). The warm SST anomalies in the central-eastern tropical Pacific gradually increase from autumn to winter of the developing year (Fig. 2a–c, g–i). During the development stage, there are no significant differences in the FD and SD composites over most

central-eastern equatorial region (Fig. 2m–o). In contrast, a clear distinction between the composite FD and SD patterns emerges during the decaying phase (Fig. 2p–r). For FD El Niño, negative SST anomalies first appear on the eastern edge of the equatorial Pacific during March–April (1) (Fig. 2d) and then extend westward gradually (Fig. 2e). In the late summer of the decaying phase (July–August (1)), statistically significant La Niña-like SST anomalies are present in the central-eastern tropical Pacific (Fig. 2f). On the contrary, during SD El Niño events the positive SST anomalies still dominate over the central-eastern tropical Pacific until July–August (1), although there are signs that the anomalies are declining in the eastern tropical Pacific (Fig. 2j–l).

Previous studies have emphasized that the subsurface ocean developing states of El Niño generally influence subsequent evolution of El Niño^{39,40}. Therefore, we investigate the difference in the subsurface ocean states between FD and SD El Niño events before the decaying phase, using the Ocean Reanalysis System 5 (ORAS5) dataset during 1958–2020 (Fig. 3). There are few statistically significant differences between FD and SD El Niño events in the central-eastern equatorial Pacific before the developing years (left panel in Fig. 3) and during the developing years (middle panel in Fig. 3), whereas the differences during the decaying years are much larger (right panel in Fig. 3). These results indicate that the developing states of FD and SD El Niño events themselves are not responsible for their different decaying rates. Thus, it is likely that external factors play crucial roles in determining the decaying phases.

As shown in Fig. 2n–r, significant differences in the SST anomalies between FD and SD El Niño events are found in the subtropical northeastern Pacific after November. Compared to the FD events, the positive SST anomalies in the subtropical northeastern Pacific during the SD cases (Fig. 2h–l) can spread equatorward and slow down the decay speeds of SST anomalies over the equatorial Pacific, via the seasonal footprinting (SF) mechanism¹⁰. Although we recognize the importance of these subtropical variations, a detailed exploration of these subtropical differences has not been provided because the primary focus of our study lies in the investigation to the Indian Ocean impact.

Evolution features of Indian Ocean SST anomalies

Here, we examine the characteristics of the Indian Ocean evolution starting from the El Niño developing autumn, as this season typically coincides with the peaking phase of the IOD. For

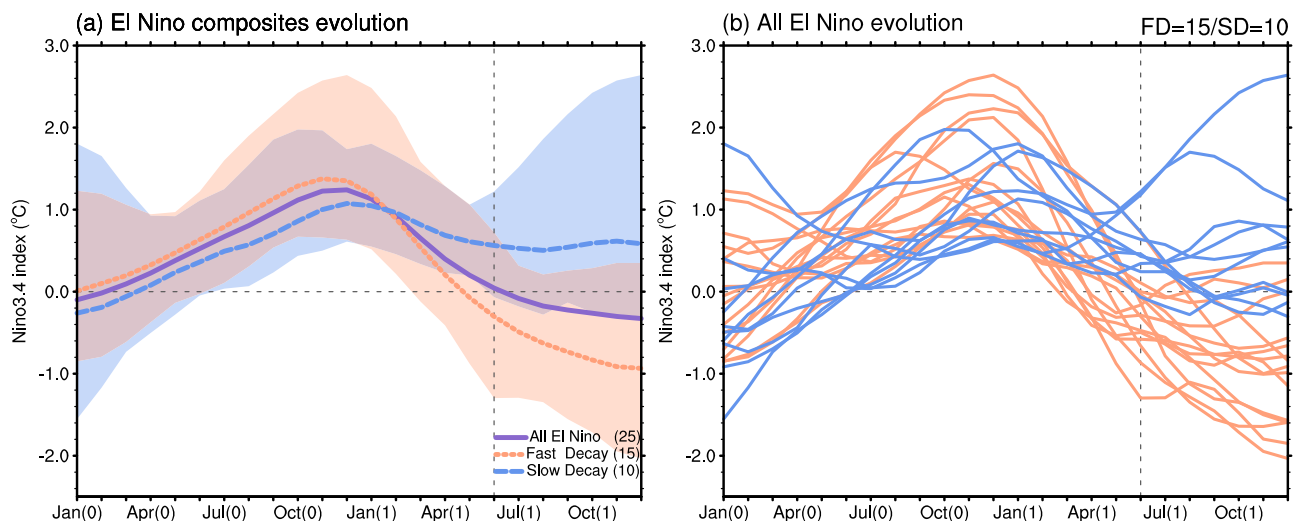


Fig. 1 Monthly evolution of Niño-3.4 index for all El Niño (purple), fast decaying (FD; orange) El Niño, and slow decaying (SD; blue) El Niño. **a** The thick curves and shading represent the average and spread of the indices, respectively. **b** The solid curves denote individual FD (orange) and SD (blue) events. “0” and “1” on the abscissa refer to the developing and decaying years of El Niño events, respectively.

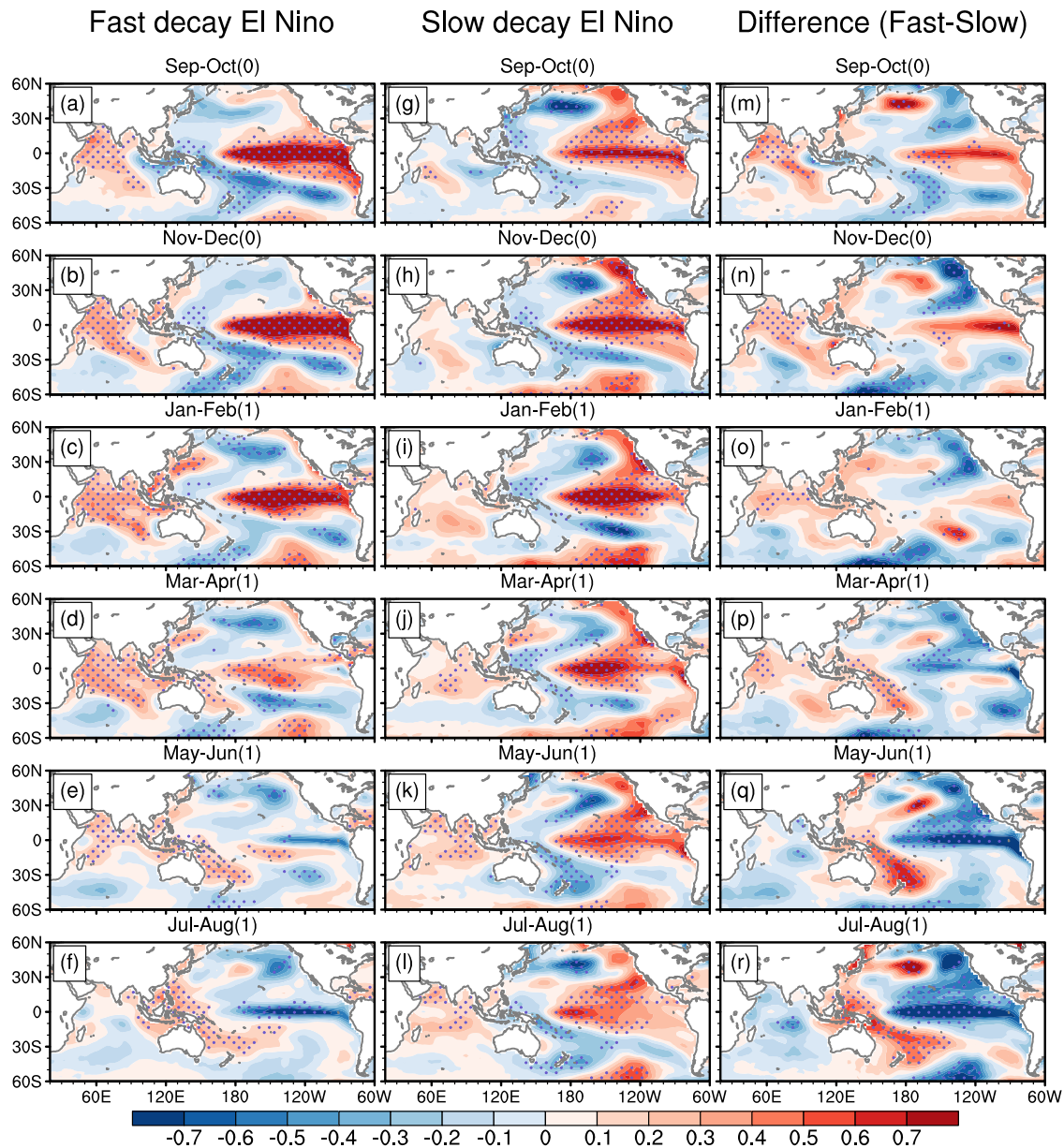


Fig. 2 Evolution of SST anomalies. Composite patterns of 2-month mean SST anomalies (shading; units: °C) for FD El Niño (a–f), SD El Niño (g–l), and differences between FD and SD El Niño (m–r) events from the developing phase to the decaying phase. Stippling indicates areas exceeding the 95% confidence level.

FD El Niño, an IOD with positive SST anomalies in the western tropical Indian Ocean and negative SST anomalies in the eastern tropical Indian Ocean peaks in September–October (0) (Fig. 2a). The intensity and spatial coverage of the SST warming in the western Indian Ocean are remarkable and much larger than those of the SST cooling in the eastern Indian Ocean. However, there is a weak IOD mode with comparable SST anomaly amplitude and extension in the eastern and western poles during SD El Niño, although it also peaks in September–October (0) (Fig. 2g).

Previous studies have indicated that both ENSO and local air-sea interaction strongly affect the initiation and evolution of different IOD types⁴¹. Moreover, Jiang et al.³² indicated that the South Asian summer monsoon could also contribute to different types of IOD. Specifically, a strong western (eastern) pole of the IOD is associated with a weak (strong) South Asian summer monsoon (SASM), while the comparable western and eastern poles develop without apparent SASM anomalies. A more

comprehensive analysis about the relative contributions of these factors is valuable, which should be addressed in the future work.

In November–December (0) during FD El Niño, there are few and insignificant signals in the eastern tropical Indian Ocean (Fig. 2b). Subsequently, the SST anomalies gradually grow into the positive IOB mode, which peaks in January–February (1) (Fig. 2c) and almost disappears in July–August (1) (Fig. 2f). This is a deviation from the typical IOB evolution, which is characterized by a peak around spring that persists into summer⁴². During SD El Niño, after the weak IOD decays in November–December (0) (Fig. 2h), the IOB pattern develops until January–February (1) (Fig. 2i), reaches its peak in May–June (1) (Fig. 2k), and persists throughout the entire summer (Fig. 2l). Overall, this suggests that an IOD with a stronger (weaker) western pole in FD (SD) El Niño events is followed by a stronger and earlier-peaking (weaker and later-peaking) IOB mode.

Because the termination of IOD is manifested as the vanishing of SST cooling in the IOD eastern pole but the SST warming still

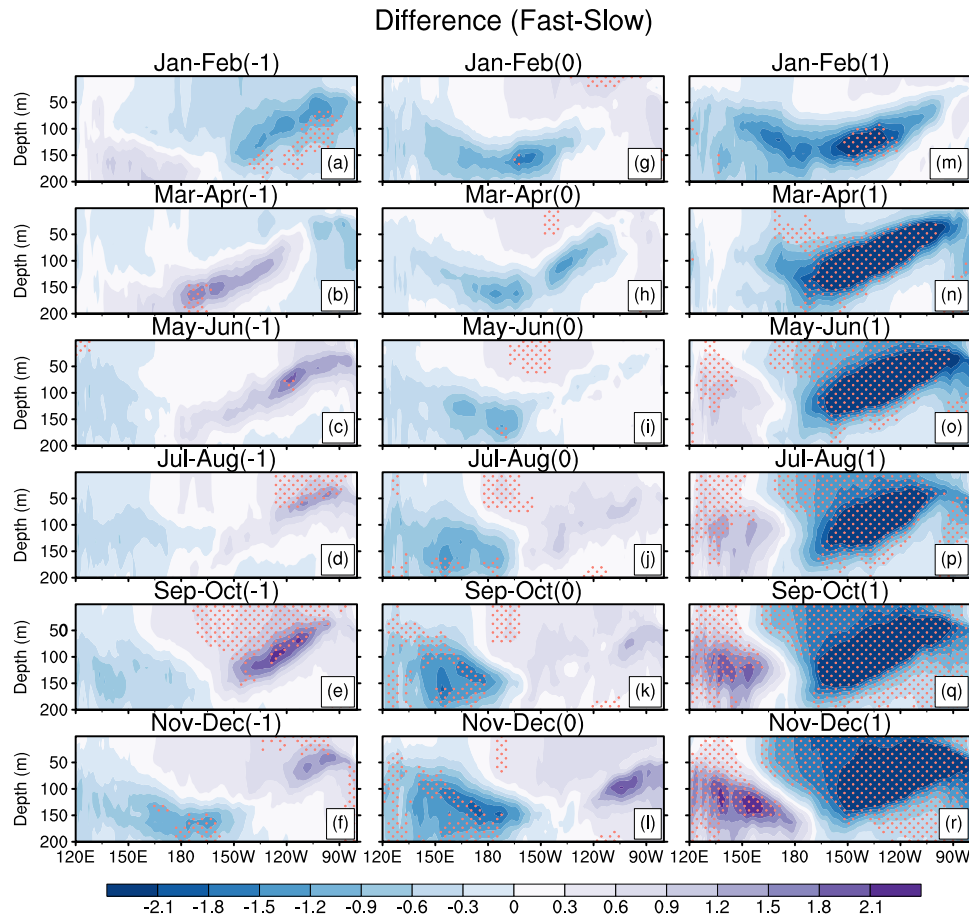


Fig. 3 Difference in ocean potential temperature anomalies between FD and SD El Niño. Depth–longitude cross-sections in the tropics (3°S – 3°N) of the differences in composite anomalies of 2-month mean ocean temperature (shading; units: $^{\circ}\text{C}$) between fast and slow decaying El Niño events before the developing years (a–f), during the developing years (g–l), and during the decaying years (m–r) based on the ORAS5 dataset for 1958–2020. Stippling denotes the significant values at the 95% confidence level.

maintains in the western Indian Ocean (Fig. 2b, h), the western pole of IOD is the initial state of the following IOB development. The IOD western pole in FD El Niño is stronger than that in SD El Niño. This phenomenon prompts us to check whether such an earlier-peaking IOB in FD El Niño is due to its faster growth or the pre-existing stronger IOD western pole. We first investigate the growth speed of the IOB mode by calculating the tendency of SST anomalies (Fig. 4). The tendency is calculated using the central time difference scheme based on the monthly time series (e.g., the tendency in September is computed by subtracting the SST anomalies in August from those in October, and then dividing the difference by 2). From September (0) to February (1), the tendency of SST anomalies in the tropical Indian Ocean is non-uniform in space, but it shows the transformation from the IOD to the IOB for both FD and SD El Niño events (Fig. 4a–c, g–i). It is noteworthy that there are no statistically significant differences in the tendency of SST anomalies between FD and SD El Niño events in most tropical Indian Ocean regions (Fig. 4m–o). In some regions, the differences (FD minus SD) are negative, meaning that the growth rates of the IOB-related SST anomalies in the FD events may be equal to or slightly slower than those in the SD events.

To quantitatively contrast the IOD and IOB developments during FD and SD El Niño events, we consider the composite evolution of Niño-3.4, IOD, and IOB indices and their tendencies (Fig. 5). From the boreal summer to winter in the El Niño developing year, the IOD indices in FD and SD cases display almost synchronous evolutions (Fig. 5b, e). However, there is a considerable difference in the peak amplitude of the IOD index,

which is mainly attributed to the stronger and broader western pole of the IOD in FD events (Fig. 2a, g). The IOB pattern in FD El Niño is stronger and shows earlier-peaking than that in SD El Niño (Fig. 5c). Interestingly, from October (0) to February (1) when the IOB develops most rapidly, the tendency of the IOB index in FD El Niño is comparable to that in SD El Niño (Fig. 5f). In October (0)–December (0), the tendency of the IOB index in FD El Niño even becomes smaller, although only slightly, than that in SD El Niño. Based on the above analysis, we can infer that the stronger and earlier-peaking IOB in FD El Niño is caused by the initial stronger and broader warm western pole of the IOD, rather than by the faster growth rates of the IOB.

Further analysis indicates that about 88% of the strong IOD western poles (7 in 8) develop into stronger and earlier-peaking IOB, while 69% of the weak western poles (9 in 13) result in late-peaking IOB (Supplementary Fig. 1). Moreover, there are four events with a moderate IOD western pole, where the difference between the intensity of their IOD western poles and the mean intensity is less than 0.1, and three-fourths of them are also followed by stronger and earlier-peaking IOB. The above results further affirm the significant contribution of the IOD western pole to IOB development.

Combined with the previously proposed IOB impacts on El Niño decay noted in the introduction, one would naturally associate the divergent decaying paces of FD and SD El Niño events with the differences in intensity and spatial distribution of the eastern and western poles of the IOD. These effects may not be facilitated directly by the physical impacts of the IOD itself, but indirectly

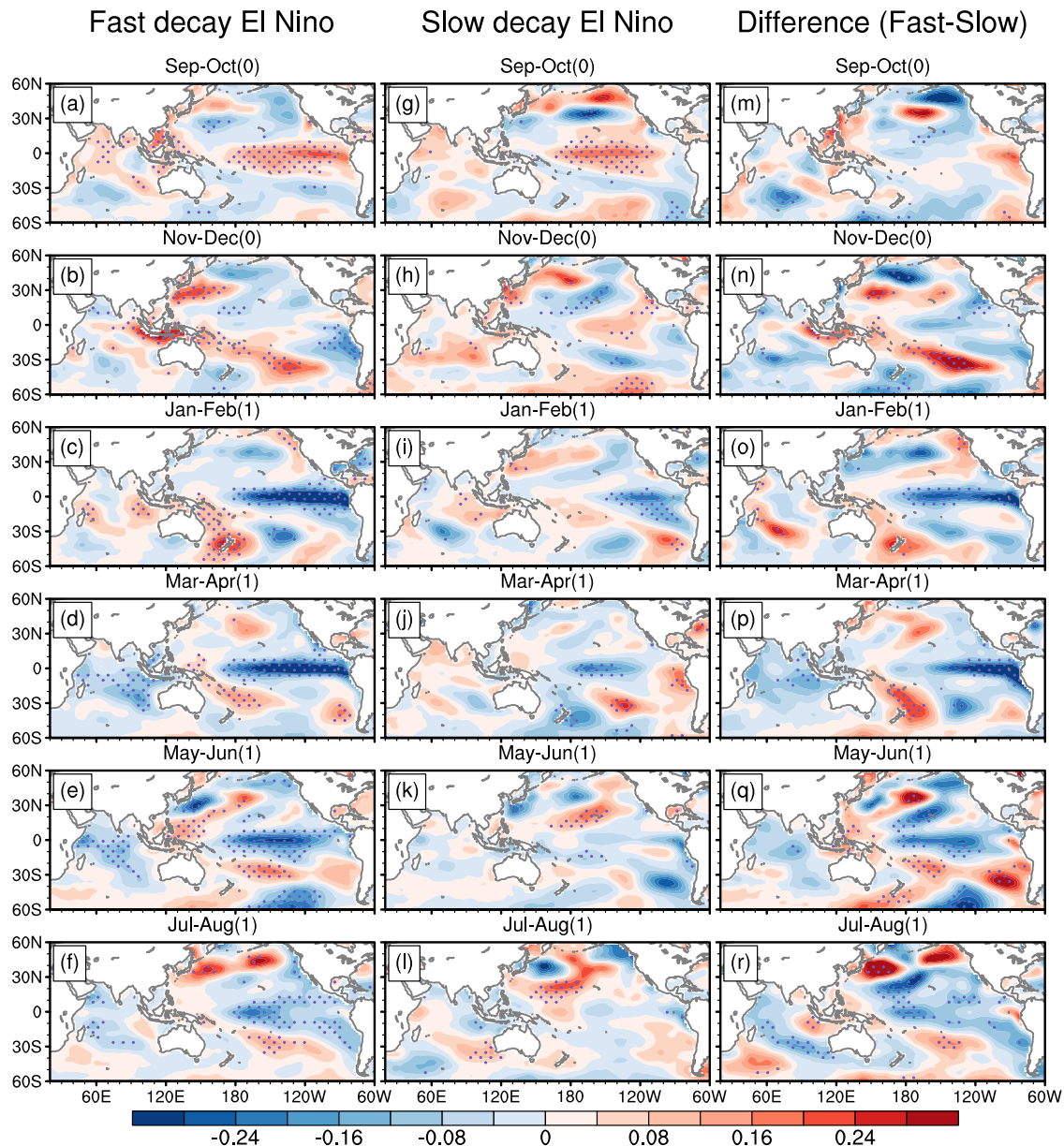


Fig. 4 Evolution of SST anomaly tendency. Same as Fig. 2, but for the tendency of SST anomalies (units: $^{\circ}\text{C month}^{-1}$).

through favoring a stronger and earlier-peaking IOB that is more conducive to El Niño decay. We will show evidence for this speculation next.

Associated physical mechanism for IOD impact on El Niño decay

To explore the physical mechanisms behind the influence of the IOD on El Niño decay, we show composite anomalies of precipitation and 850-hPa winds for FD and SD El Niño events, and the differences between composite FD and SD patterns (Fig. 6). We also show the composite equatorial zonal vertical circulation anomalies (Fig. 7). For FD El Niño, rainfall increases over the western tropical Indian Ocean but decreases over the eastern tropical Indian Ocean when the IOD peaks in September–October (0), accompanied by lower-level easterly wind anomalies over the equatorial Indian Ocean (Fig. 6a). However, the western equatorial Pacific is still dominated by the westerly wind anomalies that are conducive to the persistence of El Niño. The westerly wind anomalies also present in the SD composite pattern (Fig. 6g); and

there is essentially no statistically significant difference in wind field over the western equatorial Pacific between FD and SD cases (Fig. 6m), suggesting that there is little direct influence of the IOD on El Niño decay during September–October (0).

Based on the results in section “Results,” namely, the IOD with a stronger western pole can lead to a stronger and earlier-peaking IOB, we now investigate whether the IOD with a stronger western pole can accelerate the termination of El Niño by regulating the development of the IOB. During November–December (0) when the weak SST anomalies of the IOD eastern pole in FD El Niño disappear, the large positive SST anomalies of the western pole stretch across the entire eastern tropical Indian Ocean (Fig. 2b). This is associated with enhanced convective activity over the entire tropical Indian Ocean (Fig. 6b). Correspondingly, the anomalous ascending motions are located in the equatorial Indian Ocean (Fig. 7c, d). Besides, the anomalous descending motions emerge over the western equatorial Pacific, which is out of phase with the circulation variation in the tropical Indian Ocean. These results indicate that the positive rainfall anomalies over the Indian

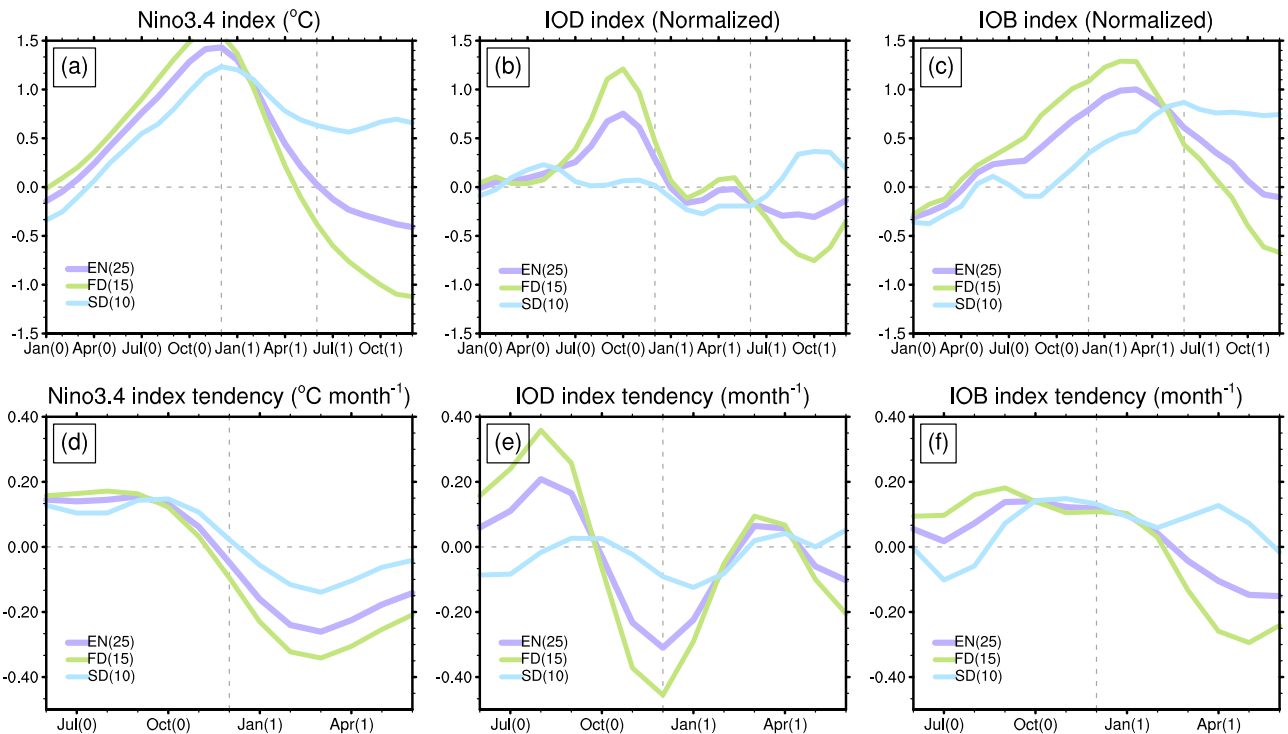


Fig. 5 Evolution of Niño-3.4, IOD and IOB indices. **a–c** Composite patterns of 3-month running mean **a** Niño-3.4 index, **b** IOD index, and **c** IOB index for all El Niño (EN; purple line), FD El Niño (green line), and SD El Niño (blue line). **d–f** Same as **(a–c)**, but for the tendency of the indices.

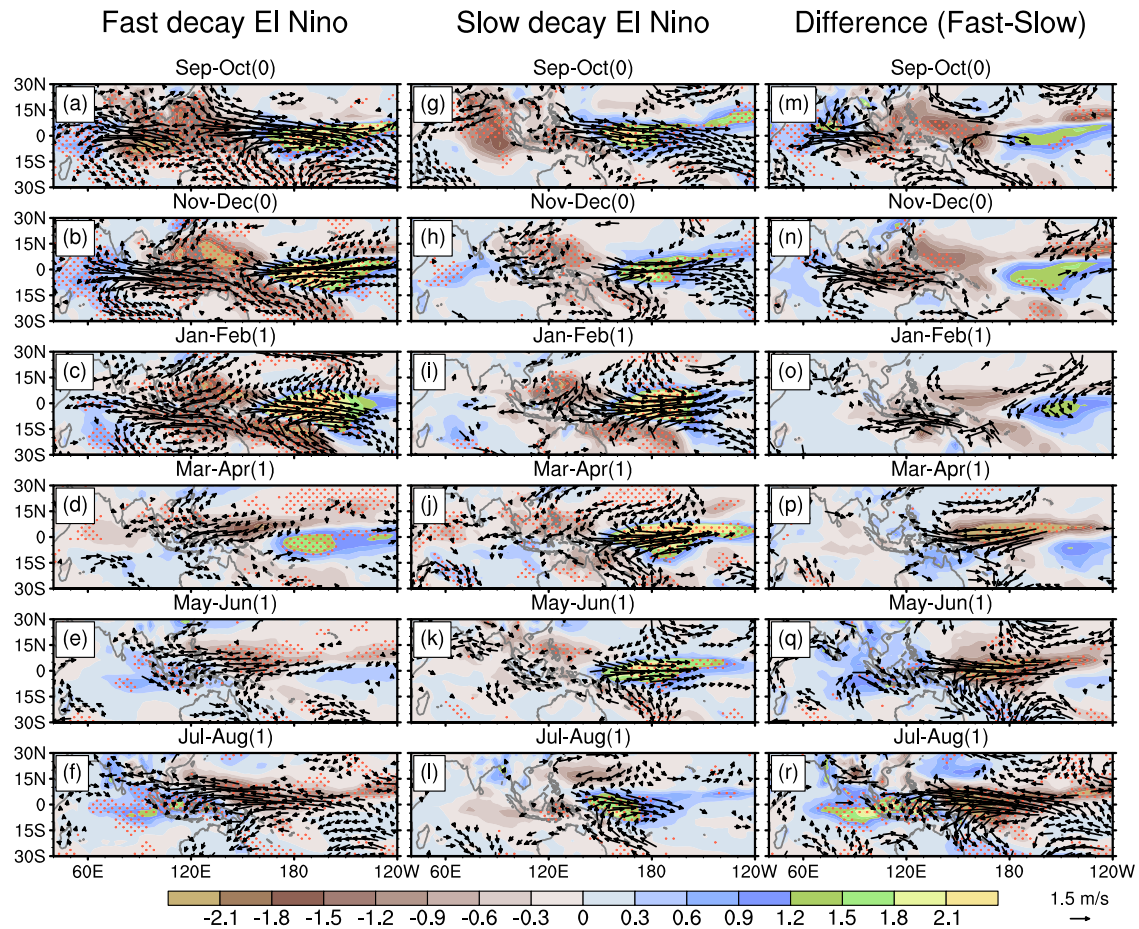


Fig. 6 Evolution of rainfall and horizontal wind anomalies. Same as Fig. 2, but for rainfall anomalies (shading; units: mm day^{-1}) and 850-hPa wind anomalies (vector; units: m s^{-1}). Only the wind vectors with wind speed significantly exceeding the 95% confidence level are plotted.

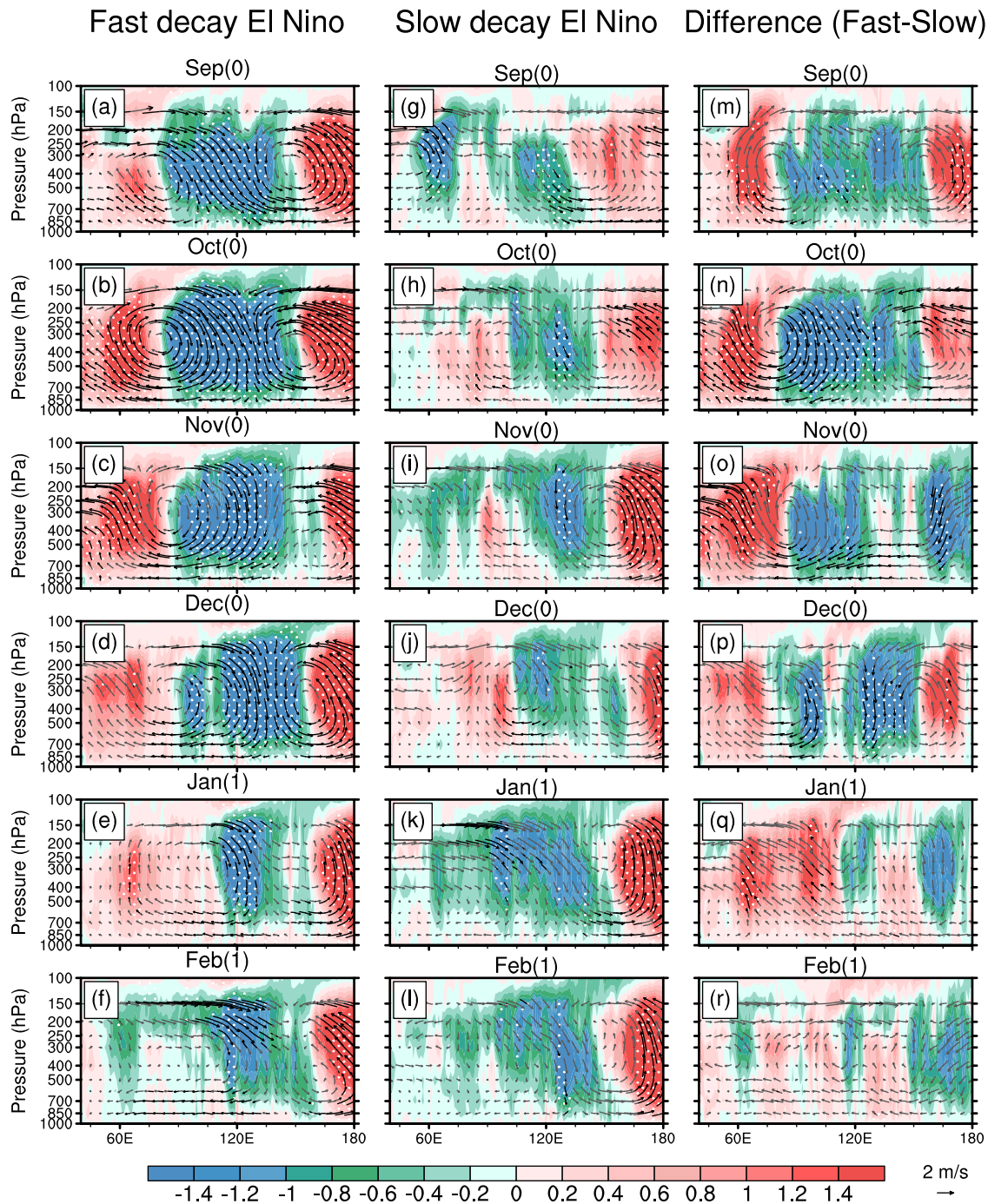


Fig. 7 Evolution of zonal vertical circulation anomalies. Composite patterns of 8°S – 8°N averaged vertical velocities (shading; units: $5 \times 10^2 \text{ Pa s}^{-1}$) and zonal vertical circulation anomalies (vector; units: m s^{-1}) for FD El Niño (a–f), SD El Niño (g–l), and the differences between FD and SD El Niño (m–r) events. Stippling and Black vectors indicates anomalous vertical velocities and wind speeds significantly exceeding the 95% confidence level, respectively.

Ocean can induce an anomalous Walker circulation with rising motions over the equatorial Indian Ocean and sinking motions over the western equatorial Pacific (Fig. 7c, d). Because the sinking center of anomalous Indo-Pacific Walker circulation during November–December (0) shifts eastward compared to that during September–October (0) (Fig. 7c, d vs. Fig. 7a, b), the lower-level easterly wind anomalies over the western flank of the sinking regions can invade the western equatorial Pacific. In the peaking phase of the IOB during January–February (1), these easterly wind anomalies intensify and extend further eastward (Fig. 6c), which

can excite the eastward-propagating oceanic upwelling Kelvin waves¹⁷. These waves shallow the thermocline depth in the eastern tropical Pacific to terminate El Niño, as demonstrated previously^{16,43}.

Note that the IOB-induced rainfall (Fig. 6d–e) and Walker circulation (Fig. 7f) anomalies almost dissipate after winter, despite the occurrence of the positive SST anomalies in the tropical Indian Ocean. The rainfall anomalies in the tropical Indian Ocean during March–April (1) are characterized by a weak north–south dipole, with negative (positive) rainfall anomalies to the north (south) of

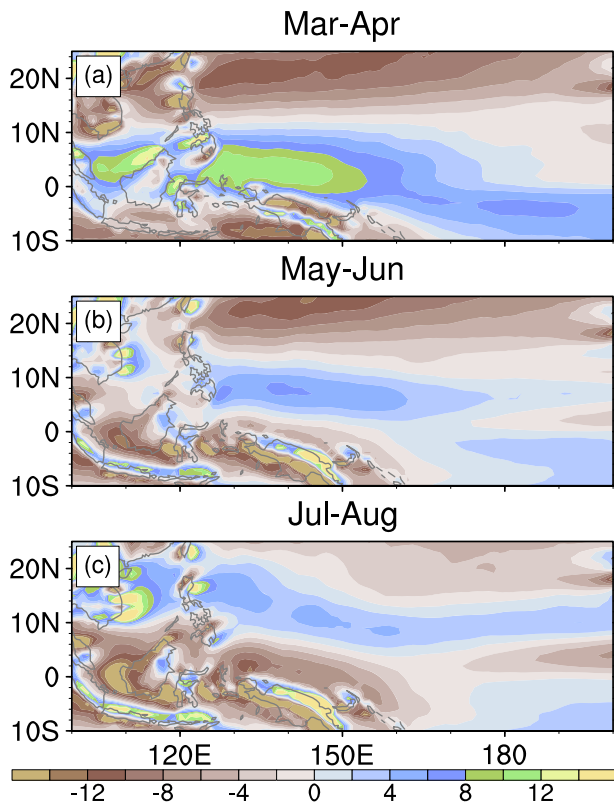


Fig. 8 Characteristics of climatological relative vorticity. Climatological 2-month mean values of 850-hPa relative vorticity (shading; units: 10^{-6} s^{-1}) during March–April (a), May–June (b) and July–August (c).

the equator (Fig. 6d), which is consistent with previous findings^{44,45}. It has been argued that such dipole rainfall anomalies rarely affect the atmospheric circulation over the western tropical Pacific⁴⁵. Furthermore, the reinforced convective activity during July–August (1) (Fig. 6f) is not caused by the IOB because the IOB has vanished by that time (Fig. 2f). Nonetheless, the IOB-induced easterly wind anomalies over the western equatorial Pacific during winter can continue to amplify, and extend eastward via local positive feedback after March (1) (Fig. 6d–f), thus providing a continuous boost to El Niño decay. From spring to summer, the climatological northwestern Pacific monsoon trough, often associated with deep convection, is located in the northern periphery of these easterly wind anomalies (Fig. 8a–c). The lower-level anomalous anticyclonic flow associated with these easterly anomalies can suppress the convection over the monsoon trough regions (Fig. 6d–f). Then, the decreased convective activity over the western tropical Pacific in turn enhances the lower-level anticyclonic anomalies that facilitate the maintenance and enhancement of easterly wind anomalies over the western Pacific. In addition, during May–June (1) the enhanced east–west SST gradient due to the occurrence of negative SST anomalies over the eastern equatorial Pacific (Fig. 2e) further reinforces easterly wind anomalies and extends them eastward via the Bjerknes positive feedback⁴⁶.

For SD El Niño, the weak IOD with comparable SSTA amplitude in the eastern and western poles also fades away during November–December (0), but the weak and insignificant SST anomalies in the western pole cannot provide sufficient warm SST background to accelerate the developing process of the IOB. Therefore, the strength of the IOB in SD El Niño is weaker and peaks later than that in FD El Niño (Fig. 2, middle panel). Even

though the IOB can persist into late summer, there are no statistically significant signals of rainfall and atmospheric circulation over the Indian Ocean to connect with the wind variation in the western equatorial Pacific (Figs. 6g–l and 7g–l). Additionally, the westerly wind anomalies over the western equatorial Pacific sustain from the peaking winter to the decaying summer (Fig. 6g–l), suggesting that the Indian Ocean SST variation in SD El Niño seem to exert little effect on circulation changes over the western tropical Pacific. Focusing on the difference between FD and SD El Niño events, the results clearly show that the easterly wind anomalies gradually intrude into the western tropical Pacific during November–December (0), and then further strengthen and extend eastward, which are caused by an eastward shift of the Indo-Pacific Walker circulation anomalies originating from the strong rising motions over the Indian Ocean in FD El Niño (right panels in Fig. 7).

DISCUSSION

This study is aimed at understanding the relationship between the IOD mode and El Niño decay. There is a statistically significant correlation between the boreal-autumn IOD and ENSO at lags 9–14 months²³; and previous studies attempted to explore the potential physical mechanisms responsible for this statistical relationship. However, the mechanisms are still controversial^{25,28}. Moreover, Jiang et al.²² proposed that the lagged IOD–ENSO correlation was merely a mathematical manifestation of ENSO autocorrelation and did not provide any additional information for ENSO prediction.

By analyzing observed FD and SD El Niño events, we demonstrate that the IOD indeed exerts a physically meaningful influence on El Niño decay, rather than merely exhibiting a statistical correlation with the ENSO in the following year. Specifically, based on the previously proposed effect of El Niño in promoting IOB warming, our study suggests that the key factor determining the strong and earlier-peaking IOB mode for FD El Niño is the preceding IOD with a strong and broad western pole (Fig. 9). Due to the similar Pacific warming and the related effect on the Indian Ocean during FD and SD El Niño events, the growth rates of the IOB are comparable for FD and SD El Niño events from November (0) to February (1). However, the IOD events in the autumn (September–October–November (SON)) of the developing years of FD and SD El Niño events are different, which provide different preconditions for the subsequent IOB development. For the IOD associated with FD El Niño, the warming of the western pole is strong, but the cooling of the eastern pole is weak. With such preconditions, the IOB can develop earlier into one with strong amplitude. This IOB in FD El Niño efficiently modulates the Walker circulation over the Indo-Pacific Ocean. Then, the resultant lower-level easterly wind anomalies over the western equatorial Pacific excite eastward propagation of downwelling Kelvin waves, thereby accelerating the termination of El Niño. In contrast, the IOD associated with SD El Niño, characterized by a weak western pole, does not provide favorable conditions for the development of the IOB. Consequently, the IOB in SD El Niño is weak and peaks later in early summer (April–May–June (AMJ)). As a result, the IOB in SD El Niño cannot induce the same physical processes as that in FD El Niño, allowing the positive SST anomalies over the central-eastern tropical Pacific to persist until the entire summer (JJA).

Therefore, the effect of the IOD on different decaying paces of El Niño is not direct via the physical impact of the IOD itself, but rather indirectly through providing preconditions that favor stronger and earlier-peaking IOB. The combined effect of the IOD and IOB has been recognized previously^{28,47}. Izumo et al.²⁸ emphasized that the abrupt demise of the IOD eastern pole was conducive to the faster development of the surface easterly wind anomalies (induced by IOB warming) over the western equatorial Pacific, compared with the sole effect of the IOB. Ha et al.⁴⁸ also

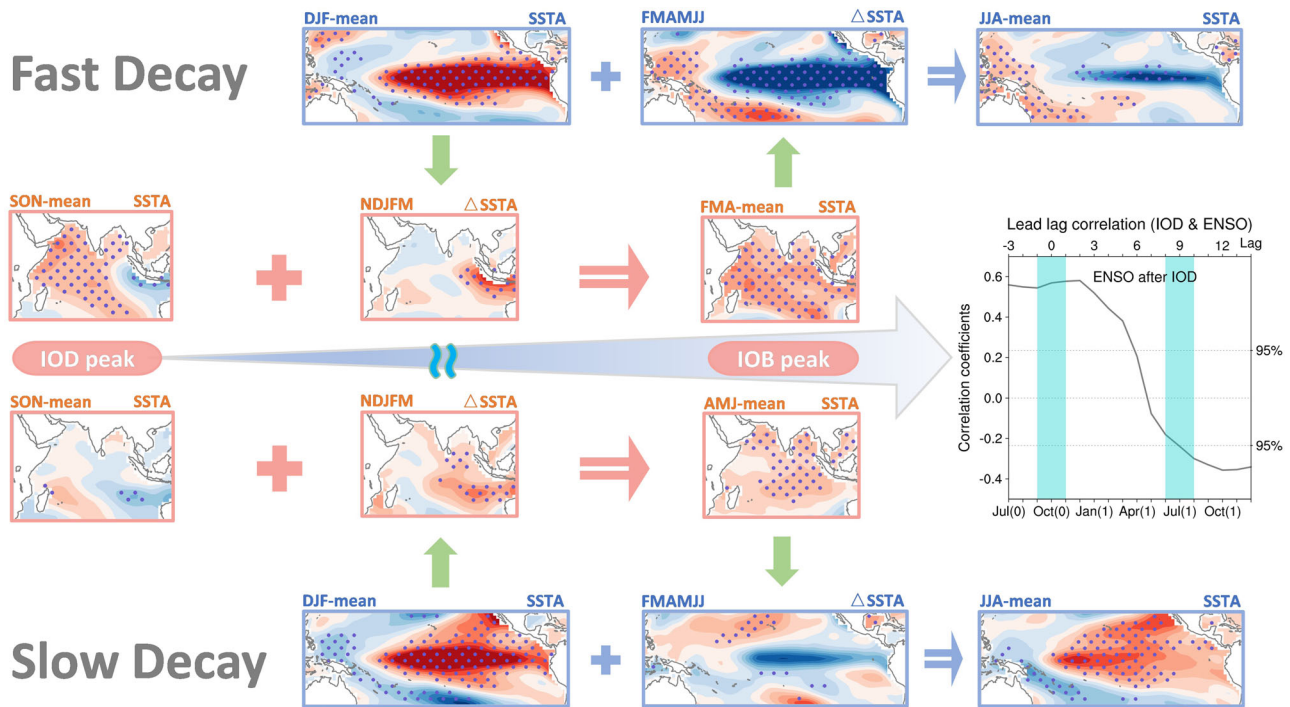


Fig. 9 Schematic diagram illustrating the influence of strong western pole of the IOD on ENSO decay. Characteristics of SST anomalies and SST anomaly tendency in the tropical Indian Ocean and Pacific Ocean are shown in figures with red and blue frames, respectively.

suggested that the faster IOD decay and the subsequent predominant IOB contributed to the rapid termination of El Niño. However, our analysis indicates that the IOD patterns in FD and SD El Niño events display almost simultaneous transition paces toward the IOB. Instead, there are huge differences in the intensity and coverage of the two poles of the IOD, which previous studies have not taken into account due to the mix of FD and SD El Niño events. Therefore, to enhance our understanding and prediction of El Niño decay, it is necessary to pay more attention to the state of the IOD, especially the western pole.

To confirm our results, we also tried to use a much larger sample size of long-term simulations from phase 6 of the Coupled Model Intercomparison Project (CMIP6) models. Unfortunately, the observed IOD with a stronger and broader western pole in FD El Niño is not well captured by the historical multi-model ensemble mean of the simulations. Instead, the simulated FD El Niño events accompany with an IOD with the stronger cooling in the eastern pole than the warming in the western pole, and even an excessive westward extension of the equatorial Indian Ocean cooling (figure not shown). The simulated IOD in SD El Niño also tends to have a stronger eastern pole than the western pole. This highlights the significant lack of realism in IOD simulations by the CMIP6 models, at least those analyzed in our study (24 models).

In this regard, the study by Li et al.⁴⁹ suggested that most CMIP5 climate models exhibit mean state biases in the Indian Ocean that resemble the interannual IOD mode observed. Specifically, the simulated climatological equatorial westerly winds over the Indian Ocean are too weak relative to the observed, accompanied by excessive (insufficient) SST and subsurface ocean temperature in the western (eastern) Indian Ocean. More importantly, these biases can be amplified through a positive Bjerknes feedback during the boreal autumn. The excessively shallow thermocline depth in the eastern equatorial Indian Ocean allows subsurface variability to strongly influence the SST here. Consequently, during El Niño the overly strong thermocline-SST feedback in the eastern Indian Ocean causes an overestimated amplitude of interannual variability of the IOD mode. It has also been shown that the IOD

simulations in the CMIP6 are persistently overly strong as in the CMIP5, and the models with lower climatological SST in the eastern Indian Ocean tend to yield a stronger IOD⁵⁰.

These analyses imply that the overly strong IOD in model simulations is likely to result in an excessively strong cooling in the eastern tropical Indian Ocean due to the overly strong thermocline-SST feedback in the eastern Indian Ocean, although this aspect has not been emphasized. This feature is consistent with our analysis results based on CMIP6 multi-model ensemble mean of the historical simulations, which show that the cooling of IOD eastern pole is stronger than the warming of the western pole in both FD and SD El Niño events. The mean state biases in the climate models not only influence the simulated IOD variability, but also potentially affect the following IOB development⁵¹ and ENSO evolution. Hence, it would be useful to assess how these biases influence El Niño decay in climate models. Furthermore, since accurate simulations of the amplitude and coverage of the two poles of the IOD are crucial for understanding the relationship between the Indian Ocean and ENSO, it is necessary to pay more attention to the reduction of the simulated mean state cold biases in the tropical Indian Ocean in order to obtain dependable predictions of ENSO evolution.

METHODS

Datasets

The monthly mean datasets used in this study include: (1) the SST data ($2^\circ \times 2^\circ$) from the National Oceanic and Atmospheric Administration (NOAA) Extended Reconstructed SST version 5 (ERSSTv5)⁵²; (2) the atmospheric reanalysis data ($1^\circ \times 1^\circ$) from the European Centre for Medium-range Weather Forecasts (ECMWF) ERA5 reanalysis⁵³; (3) the precipitation data ($2.5^\circ \times 2.5^\circ$) from the global precipitation reconstruction data (PREC)⁵⁴; and (4) the ocean reanalysis datasets ($1^\circ \times 1^\circ$) from the ECMWF ORAS5 from 1958 to 2020⁵⁵. The analysis period of the above-mentioned data is from 1950 to 2020, unless otherwise specified.

Table 1. Classification of fast and slow decaying El Niño events from 1950 to 2020.

	Fast decay	Slow decay
El Niño	1951–1952, 1953–1954, 1963–1964, 1969–1970, 1972–1973, 1977–1978, 1982–1983, 1987–1988, 1994–1995, 1997–1998, 2002–2003, 2004–2005, 2006–2007, 2009–2010, 2015–2016	1957–1958, 1958–1959, 1965–1966, 1968–1969, 1976–1977, 1979–1980, 1986–1987, 1991–1992, 2014–2015, 2018–2019

Methods

Following the NOAA Climate Prediction Center, an El Niño event is identified when the three-month running mean Niño-3.4 index (area-averaged SST anomalies in 170°–120°W, 5°S–5°N)⁵⁶ exceeds 0.5 °C for 5 consecutive months or longer. To classify fast and slow decaying El Niño events, two criteria are conducted. One is that the difference in the Niño-3.4 index between the peak season and the following summer (JJA) is larger than 1 °C. The other is that the JJA Niño-3.4 index in the decaying year is smaller than or equal to 0.2 °C to ensure the recovery of the non-El Niño state. The cases that meet the two criteria are classified as FD El Niño events; otherwise, they are the SD events. The JJA Niño-3.4 SST anomalies in 1983 were approximately equal to 0.3 °C, but the difference described by the first criterion was much larger than 1 °C. The peak intensity of the El Niño in 2004 was small (0.7 °C), and failed to satisfy the first criterion. However, the tropical Pacific already turned into a normal state in the summer of the decaying year. Therefore, these two cases are also defined as FD El Niño events. Note that the category of these two cases does not change our main results. Fifteen FD cases and ten SD cases are identified for the period from 1950 to 2020 (see Table 1). It should be cautioned that there exist several consecutive El Niño events (1957–1959, 1968–1970, 1976–1978, 1986–1988, and 2014–2016) during 1950–2020. We have also conducted an analysis excluding these events (Supplementary Fig. 2 and Fig. 3) to examine the potential uncertainty. The consistent finding from this additional analysis affirms the robustness of our main conclusions.

The IOD index is defined as the difference in SST anomalies between the IOD western pole region (50°–70°E, 10°S–10°N) and eastern pole region (90°–110°E, 10°S–0°)⁵⁷. The IOB index is derived from the area-averaged SST anomalies in the tropical Indian Ocean (40°–100°E, 20°S–20°N)⁵⁸. We also apply the EOF analysis on the Indian Ocean SST anomalies in the region of 40°–120°E, 20°S–20°N to identify the IOD and IOB modes⁵⁹, and the main conclusions remain the same. The statistical significance of the results obtained is evaluated by using the two-tailed Student's *t* test.

DATA AVAILABILITY

The ERSSTv5 and PREC monthly rainfall datasets were downloaded from the NOAA (<https://psl.noaa.gov/data/gridded/data.noaa.ersst.v5.html> and <https://psl.noaa.gov/data/gridded/data.prec.html>). The ORAS5 datasets can be obtained from <https://cds.climate.copernicus.eu/cdsapp#!/dataset/10.24381/cds.67e8eeb7?tab=overview>. The ERA5 and CMIP6 datasets are publicly available online (<https://cds.climate.copernicus.eu/#/search?text=ERA5&type=dataset> and <https://esgf-node.lnl.gov/projects/cmip6/>).

CODE AVAILABILITY

The codes used for producing all figures and for computing the indices reported in this paper are available from the corresponding author upon request.

Received: 16 September 2023; Accepted: 15 December 2023;
Published online: 03 January 2024

REFERENCES

- Li, Y. et al. Different evolutions of the Philippine Sea anticyclone for the impact of El Niño in peak phases with and without a positive Indian Ocean Dipole. *J. Trop. Meteorol.* **21**, 23–33 (2015).
- Chen, M., Li, T., Shen, X. & Wu, B. Relative roles of dynamic and thermodynamic processes in causing evolution asymmetry between El Niño and La Niña. *J. Clim.* **29**, 2201–2220 (2016).
- Zhan, H. Y., Chen, R. D. & Lan, M. Interdecadal change in the interannual variation of the western edge of the western North Pacific subtropical high during early summer and the influence of tropical sea surface temperature. *J. Trop. Meteorol.* **28**, 57–70 (2022).
- Hoerling, M. & Kumar, A. The perfect ocean for drought. *Science* **299**, 691–694 (2003).
- Chowdary, J. S. et al. Indian summer monsoon rainfall variability in response to differences in the decay phase of El Niño. *Clim. Dyn.* **48**, 2707–2727 (2017).
- Jiang, W. et al. Northwest Pacific anticyclonic anomalies during post-El Niño summers determined by the pace of El Niño decay. *J. Clim.* **32**, 3487–3503 (2019).
- Larkin, N. K. & Harrison, D. E. ENSO warm (El Niño) and cold (La Niña) event life cycles: Ocean surface anomaly patterns, their symmetries, asymmetries, and implications. *J. Clim.* **15**, 1118–1140 (2002).
- McPhaden, M. J. & Zhang, X. Asymmetry in zonal phase propagation of ENSO sea surface temperature anomalies. *Geophys. Res. Lett.* **36**, L13703 (2009).
- Ohba, M. & Ueda, H. Role of nonlinear atmospheric response to SST on the asymmetric transition process of ENSO. *J. Clim.* **22**, 177–192 (2009).
- Chen, J. et al. Tropical and subtropical Pacific sources of the asymmetric El Niño–La Niña decay and their future changes. *Geophys. Res. Lett.* **49**, e2022GL097751 (2022).
- Cai, W. et al. Pantropical climate interactions. *Science* **363**, eaav4236 (2019).
- Wang, C. Three-ocean interactions and climate variability: a review and perspective. *Clim. Dyn.* **53**, 5119–5136 (2019).
- Yu, J. Y., Mechoso, C. R., McWilliams, J. C. & Arakawa, A. Impacts of the Indian Ocean on the ENSO cycle. *Geophys. Res. Lett.* **29**, 1204 (2002).
- Kug, J. S., Kirtman, B. P. & Kang, I. S. Interactive feedback between ENSO and the Indian Ocean in an interactive ensemble coupled model. *J. Clim.* **19**, 6371–6381 (2006).
- Ohba, M. & Ueda, H. An impact of SST anomalies in the Indian Ocean in acceleration of the El Niño to La Niña transition. *J. Meteorol. Soc. Jpn.* **85**, 335–348 (2007).
- Huang, R., Zhang, R. & Yan, B. Dynamical effect of the zonal wind anomalies over the tropical western Pacific on ENSO cycles. *Sci. China Ser. D Earth Sci.* **44**, 1089–1098 (2001).
- Okumura, Y. M. & Deser, C. Asymmetry in the duration of El Niño and La Niña. *J. Clim.* **23**, 5826–5843 (2010).
- Xie, S. P. et al. Indian Ocean capacitor effect on Indo-Western Pacific climate during the summer following El Niño. *J. Clim.* **22**, 730–747 (2009).
- Okumura, Y. M., Ohba, M., Deser, C. & Ueda, H. A proposed mechanism for the asymmetric duration of El Niño and La Niña. *J. Clim.* **24**, 3822–3829 (2011).
- Ohba, M. & Watanabe, M. Role of the Indo-Pacific interbasin coupling in predicting asymmetric ENSO transition and duration. *J. Clim.* **25**, 3321–3335 (2012).
- Jourdain, N. C., Lengaigne, M., Vialard, J., Izumo, T. & Gupta, A. S. Further insights on the influence of the Indian Ocean Dipole on the following year's ENSO from observations and CMIP5 models. *J. Clim.* **29**, 637–658 (2016).
- Jiang, F., Zhang, W., Jin, F. F., Stuecker, M. F. & Allan, R. El Niño pacing orchestrates inter-basin Pacific-Indian Ocean interannual connections. *Geophys. Res. Lett.* **48**, e2021GL095242 (2021).
- Izumo, T. et al. Influence of the state of the Indian Ocean Dipole on the following years El Niño. *Nat. Geosci.* **3**, 168–172 (2010).
- Izumo, T. et al. Influence of Indian Ocean Dipole and Pacific recharge on following year's El Niño: interdecadal robustness. *Clim. Dyn.* **42**, 291–310 (2014).
- Dayan, H., Izumo, T., Vialard, J., Lengaigne, M. & Masson, S. Do regions outside the tropical Pacific influence ENSO through atmospheric teleconnections? *Clim. Dyn.* **45**, 583–601 (2015).
- Annamalai, H., Xie, S. P., McCreary, J. P. & Murtugudde, R. Impact of Indian Ocean sea surface temperature on developing El Niño. *J. Clim.* **18**, 302–319 (2005).
- Annamalai, H., Kida, S. & Hafner, J. Potential impact of the tropical Indian Ocean-Indonesian seas on El Niño characteristics. *J. Clim.* **23**, 3933–3952 (2010).
- Izumo, T., Vialard, J., Dayan, H., Lengaigne, M. & Suresh, I. A simple estimation of equatorial Pacific response from windstress to untangle Indian Ocean Dipole and Basin influences on El Niño. *Clim. Dyn.* **46**, 2247–2268 (2016).

29. Yang, S., Ding, X., Zheng, D. & Yoo, S. H. Time-frequency characteristics of the relationships between tropical Indo-Pacific SSTs. *Adv. Atmos. Sci.* **24**, 343–359 (2007).
30. Sun, S., Fang, Y., Tana & Liu, B. Dynamical mechanisms for asymmetric SSTA patterns associated with some Indian Ocean Dipoles. *J. Geophys. Res. Oceans* **119**, 3076–3097 (2014).
31. Cai, W. et al. Opposite response of strong and moderate positive Indian Ocean Dipole to global warming. *Nat. Clim. Chang.* **11**, 27–32 (2021).
32. Jiang, J. et al. Three types of positive Indian Ocean Dipoles and their relationships with the South Asian summer monsoon. *J. Clim.* **35**, 405–424 (2022).
33. Zhao, X., Yuan, D., Yang, G., Zhou, H. & Wang, J. Role of the oceanic channel in the relationships between the basin/dipole mode of SST anomalies in the tropical Indian Ocean and ENSO transition. *Adv. Atmos. Sci.* **33**, 1386–1400 (2016).
34. Yoo, J. H., Moon, S., Ha, K. J., Yun, K. S. & Lee, J. Y. Cases for the sole effect of the Indian Ocean Dipole in the rapid phase transition of the El Niño–Southern Oscillation. *Theor. Appl. Climatol.* **141**, 999–1007 (2020).
35. Alexander, M. A. et al. The atmospheric bridge: the influence of ENSO teleconnections on air–sea interaction over the global oceans. *J. Clim.* **15**, 2205–2231 (2002).
36. Lau, N. C. & Nath, M. J. Coupled GCM simulation of atmosphere–ocean variability associated with zonally asymmetric SST changes in the tropical Indian Ocean. *J. Clim.* **17**, 245–265 (2004).
37. Shinoda, T., Alexander, M. A. & Hendon, H. H. Remote response of the Indian Ocean to interannual SST variations in the tropical Pacific. *J. Clim.* **17**, 362–372 (2004).
38. Song, X., Zhang, R. & Rong, X. Dynamic causes of ENSO decay and its asymmetry. *J. Clim.* **35**, 445–462 (2022).
39. Wyrtki, K. Water displacements in the Pacific and the genesis of El Niño cycles. *J. Geophys. Res.* **90**, 7129–7132 (1985).
40. Jin, F. F. An equatorial ocean recharge paradigm for ENSO. Part I: Conceptual model. *J. Atmos. Sci.* **54**, 811–829 (1997).
41. Guo, F., Liu, Q., Sun, S. & Yang, J. Three types of Indian Ocean Dipoles. *J. Clim.* **28**, 3073–3092 (2015).
42. Guo, F., Liu, Q., Yang, J. & Fan, L. Three types of Indian Ocean Basin modes. *Clim. Dyn.* **51**, 4357–4370 (2018).
43. Weisberg, R. H. & Wang, C. A western Pacific oscillator paradigm for the El Niño–Southern Oscillation. *Geophys. Res. Lett.* **24**, 779–782 (1997).
44. Wu, R., Kirtman, B. P. & Krishnamurthy, V. An asymmetric mode of tropical Indian Ocean rainfall variability in boreal spring. *J. Geophys. Res.* **113**, D05104 (2008).
45. Li, T. et al. Theories on formation of an anomalous anticyclone in western North Pacific during El Niño: a review. *J. Meteorol. Res.* **31**, 987–1006 (2017).
46. Bjerknes, J. Atmospheric teleconnections from the equatorial Pacific. *Mon. Weather Rev.* **97**, 163–172 (1969).
47. Hong, C.-C., Li, T., LinHo & Chen, Y. C. Asymmetry of the Indian Ocean basinwide SST anomalies: roles of ENSO and IOD. *J. Clim.* **23**, 3563–3576 (2010).
48. Ha, K. J., Chu, J. E., Lee, J. Y. & Yun, K. S. Interbasin coupling between the tropical Indian and Pacific Ocean on interannual timescale: observation and CMIP5 reproduction. *Clim. Dyn.* **48**, 459–475 (2017).
49. Li, G., Xie, S. P. & Du, Y. Monsoon-induced biases of climate models over the tropical Indian Ocean. *J. Clim.* **28**, 3058–3072 (2015).
50. McKenna, S., Santoso, A., Gupta, A. S., Taschetto, A. S. & Cai, W. Indian Ocean Dipole in CMIP5 and CMIP6: characteristics, biases, and links to ENSO. *Sci. Rep.* **10**, 11500 (2020).
51. Li, G., Xie, S. P. & Du, Y. Climate model errors over the South Indian Ocean thermocline dome and their effect on the basin mode of interannual variability. *J. Clim.* **28**, 3093–3098 (2015).
52. Huang, B. et al. Extended reconstructed Sea surface temperature, Version 5 (ERSSTv5): Upgrades, validations, and intercomparisons. *J. Clim.* **30**, 8179–8205 (2017).
53. Hersbach, H. et al. The ERA5 global reanalysis. *Q. J. R. Meteorol. Soc.* **146**, 1999–2049 (2020).
54. Chen, M., Xie, P., Janowiak, J. E. & Arkin, P. A. Global land precipitation: a 50-yr monthly analysis based on gauge observations. *J. Hydrometeorol.* **3**, 249–266 (2002).
55. Zuo, H., Balmaseda, M. A., Tietsche, S., Mogensen, K. & Mayer, M. The ECMWF operational ensemble reanalysis–analysis system for ocean and sea ice: a description of the system and assessment. *Ocean Sci.* **15**, 779–808 (2019).
56. Rayner, N. A. et al. Global analyses of sea surface temperature, sea ice, and night marine air temperature since the late nineteenth century. *J. Geophys. Res.* **108**, 4407 (2003).
57. Saji, N. H., Goswami, B. N., Vinayachandran, P. N. & Yamagata, T. A dipole mode in the tropical Indian Ocean. *Nature* **401**, 360–363 (1999).
58. Zheng, X. T., Xie, S. P. & Liu, Q. Response of the Indian Ocean Basin mode and its capacitor effect to global warming. *J. Clim.* **24**, 6146–6164 (2011).
59. Chu, J. E. et al. Future change of the Indian Ocean basin-wide and dipole modes in the CMIP5. *Clim. Dyn.* **43**, 535–551 (2014).

ACKNOWLEDGEMENTS

This study was supported by the National Natural Science Foundation of China (Grant 42088101), the Guangdong Province Key Laboratory for Climate Change and Natural Disaster Studies (Grant 2020B1212060025), and the Southern Marine Science and Engineering Guangdong Laboratory (Zhuhai) (Grant SML2021SP302). N.K. acknowledges funding from the NFR COMBINED (Grant 328935) and NFR ROADMAP project (Grant 316618). The BCPU hosted J.W. visit to University of Bergen (Trond Mohn Foundation Grant BFS2018TMT01).

AUTHOR CONTRIBUTIONS

Conceptualization: J.W., H.F., and S.Y.; methodology: J.W., H.F., and W.Z.; visualization: J.W.; result analysis: J.W., H.F., S.Y., S.L., S.H., and N.K.; writing manuscript: J.W., S.Y., and H.F. All authors read and approved the final manuscript.

COMPETING INTERESTS

The authors declare no competing interests.

ADDITIONAL INFORMATION

Supplementary information The online version contains supplementary material available at <https://doi.org/10.1038/s41612-023-00554-5>.

Correspondence and requests for materials should be addressed to Song Yang.

Reprints and permission information is available at <http://www.nature.com/reprints>

Publisher's note Springer Nature remains neutral with regard to jurisdictional claims in published maps and institutional affiliations.



Open Access This article is licensed under a Creative Commons Attribution 4.0 International License, which permits use, sharing, adaptation, distribution and reproduction in any medium or format, as long as you give appropriate credit to the original author(s) and the source, provide a link to the Creative Commons license, and indicate if changes were made. The images or other third party material in this article are included in the article's Creative Commons license, unless indicated otherwise in a credit line to the material. If material is not included in the article's Creative Commons license and your intended use is not permitted by statutory regulation or exceeds the permitted use, you will need to obtain permission directly from the copyright holder. To view a copy of this license, visit <http://creativecommons.org/licenses/by/4.0/>.

© The Author(s) 2024